Suppressing artificial equilibrium states caused by spurious currents in droplet spreading simulations with dynamic contact angle model

Thomas Antritter*

Institute for Technical Thermodynamics,
Technische Universität Darmstadt,
Alarich-Weiss-Str. 10, 64287 Darmstadt, Germany
Email: antritter@ttd.tu-darmstadt.de
*Corresponding author

Martin Mayer and Peter Hachmann

Research and Development,
Heidelberger Druckmaschinen AG,
Gutenbergring, 69168 Wiesloch, Germany
Email: martin.mayer@heidelberg.com
Email: peter.hachmann@heidelberg.com

Martin Wörner

Karlsruhe Institute of Technology (KIT),
Institute of Catalysis Research and Technology,
Engesserstr. 20, 76131 Karlsruhe, Germany,
Email: martin.woerner@kit.edu

Abstract: Accurate methods for numerical simulation of dynamic wetting and spreading phenomena are a valuable tool to support the advancement of related technological processes such as inkjet-printing. Here, it is demonstrated that numerical methods employing dynamic contact angle models are prone to artificial equilibrium states caused by spurious (parasitic) currents. The capability of different approaches in reducing spurious currents for sessile and spreading droplets with low equilibrium contact angle is evaluated. To minimise the influence of spurious currents on dynamic contact angle models, a smoothing step in the evaluation of the contact line velocity is introduced in this paper. The benefit and performance of this new approach is demonstrated by algebraic volume-of-fluid simulations of spreading and receding droplets with the Kistler dynamic contact angle model.

Keywords: droplet; wetting; spreading; inkjet printing; dynamic contact angle; spurious currents; parasitic currents; numerical simulation; volume-of-fluid method; OpenFOAM.

Reference to this paper should be made as follows: Antritter, T., Mayer, M., Hachmann, P. and Wörner, M. (2020) 'Suppressing artificial equilibrium states caused by spurious currents in droplet spreading simulations with dynamic contact angle model', *Progress in Computational Fluid Dynamics*, Vol. 20, No. 2, pp.59–70.

Biographical notes: Thomas Antritter studied Mechanical Engineering at the Karlsruhe Institute of Technology (KIT), Germany. Since his graduation as Master of Science in 2017, he has been continuing his work on the numerical simulation of wetting phenomena at the Institute for Technical Thermodynamics of Technische Universität Darmstadt.

Martin Mayer received his Master in Mechanical Engineering from University Karlsruhe, Germany in 1988 and his Master in Business Administration from New Hampshire College, USA in 1997. Since 1997, he is a Senior Engineer at R&D at Heidelberger Druckmaschinen AG with focus of work on measuring, modelling and controlling of fluid metering processes in digital and offset printing.

Peter Hachmann received his PhD in Technical Science from the Swiss Federal Institute of Technology (ETH) Zurich in 1997. He is the Head of the Department 'Inkjet Competence' of Heidelberger Druckmaschinen AG, Germany, where he and his team are doing R&D work on inkjet topics namely inkjet processes, inks and heads.

Martin Wörner received his PhD in Mechanical Engineering from University Karlsruhe, Germany, in 1994. He is the Head of the Multiphase Flow Group at Institute of Catalysis Research and Technology (IKFT) of Karlsruhe Institute of Technology (KIT), Germany, where he is also teaching on numerical modelling of multiphase flows.

1 Introduction

Droplet impact and spreading are key elements to many technical applications, such as inkjet printing, fuel spray injection or spray cooling. Therefore, they have continuously been in the focus of research efforts (Josserand and Thoroddsen, 2016). Numerical simulations have contributed to develop a better understanding of the underlying processes. Capturing the hydrodynamics in the three phase region correctly can thereby be essential for accurately describing the macroscopic flow and heat transfer. However, for engineering applications the micro region usually can not be sufficiently resolved due to the computational cost caused by the necessary mesh resolution. A common approach to overcome this issue is to model the apparent macroscopic dynamic contact angle as function of the velocity of the advancing or receding contact line.

When a droplet is posed on a substrate it usually is at first not in its thermodynamic equilibrium as described by the Young-Dupré equation. The contact line will therefore move towards the equilibrium state. The hydrodynamics of contact line motion have been studied extensively in the past. A review can be found in Bonn et al. (2009). Tanner (1979) experimentally examined the spreading of silicone oil drops on glass and found a correlation between the dynamic apparent contact angle θ_d and the capillary number of contact line motion $Ca = \mu u_\mathrm{cl}/\sigma$. Here, u_cl is the velocity of the contact line, μ the dynamic liquid viscosity and σ the coefficient of surface tension. Assuming the existence of a precursor film and Stokes flow in the vicinity of the contact line, Tanner derived for completely wetting systems the relation $\tan(\theta_\mathrm{d}) \propto \sqrt[3]{Ca}$. For small θ_d and therefore small Ca, this relation can be simplified to $\theta_\mathrm{d} \propto \sqrt[3]{Ca}$. Other, more general models describing the dynamic contact angle as function of Ca have been proposed as well in the past. An example is the model of Kistler (1993) which is widely used in literature (Šikalo et al., 2005; Muradoglu and Tasoglu, 2010; Linder et al., 2015) and is also employed in the present study.

The discussed interplay between dynamic contact angle and contact line speed governs the spontaneous spreading of small droplets. The well-known Tanner law (1979), which is derived from the above contact angle model, describes the time evolution of the contact line diameter (d_cl) of a spreading droplet as $d_\mathrm{cl} \propto t^{0.1}$. It has been validated for a multitude of fluid-substrate systems (Bonn et al., 2009). Consequently, it is crucial to incorporate dynamic contact angle models in the numerical simulation of droplet impingement and spreading in order to appropriately model the underlying physics. Yet, the calculation of the velocity of propagation of the contact line u_cl poses a challenging task and various methods are used in literature, see, e.g., Malgarinos et al. (2015) for a recent overview. A rather straight forward approach often adopted in sharp interface methods such as the geometrical volume-of-fluid method (Bussmann et al., 1999), the coupled level-set volume-of-fluid method (Yokoi et al., 2009) and the front-tracking method (Muradoglu and Tasoglu, 2010) is to use the velocity components tangential to the wall at the nearest node or marker point as the contact line velocity. For numerical methods with smeared/smoothed interface representation such as the algebraic/colour-function volume-of-fluid method (CF-VOF) or the phase-field method it is difficult to calculate the contact line velocity since in general a reconstruction of the contact line is missing in those methods. Therefore, a velocity evaluated from the local velocity field in the vicinity of the contact line is used to estimate u_cl instead. For the CF-VOF method, such approximations are employed, e.g., by Berberović (2010) and Dupont and Legendre (2010).

Both, the Tanner model and the Kistler model predict a strong increase of θ_d for small values of the capillary number (cf. Figure 1 in Subsection 2.4). Hence, depending on drop viscosity and surface tension, already small contact line velocities may result in a large deviation of θ_d from θ_e. As a consequence, dynamic contact angle models can react very sensitive to spurious or parasitic currents. These are artificial velocities which may arise for one or more of the following reasons:

1. an inconsistent discretisation of surface tension and pressure forces (Popinet and Zaleski, 1999)
2. the approximate solution of the pressure Poisson equation (Yokoi, 2014)
3. errors in the approximated interface curvature.

Lafaurie et al. (1994) found that for their VOF-based method called 'SURFER' the Reynolds number $Re_\mathrm{sc} = \rho u_\mathrm{sc} R/\mu$ calculated from density ρ, bubble/drop radius R and magnitude of spurious currents u_sc is proportional to the Laplace number $La = \sigma\rho R/\mu^2$. After expanding with $\mu/\rho u R$, where u is the magnitude of physical velocities, this leads to $u_\mathrm{sc}/u \propto \sigma/\mu u$ meaning that for small capillary numbers the spurious velocities become large compared to the physical flow. Hence, spurious currents can be expected to be critical especially when simulating two phase flows at low capillary numbers, such as spreading droplets.

In combination with the above mentioned sensitivity of dynamic contact angle models, spurious currents can falsify the spreading simulation. To dampen the influence of such velocity fluctuations, Bussmann et al. (1999) introduced a threshold value for u_cl so that the dynamic contact angle model is only applied above a certain magnitude of the contact line velocity. This method has, however, the drawback that below this threshold value a static contact angle is applied. In this paper we show that for applications like inkjet printing, where typically a broad spreading and thus low contact angles are desired, the interplay between spurious currents and dynamic contact angle model can even result in artificial equilibrium states. In order to suppress these, we propose a more appropriate remedy than introducing a cutoff velocity for the contact angle model, namely an additional smoothing step in the evaluation of the contact line velocity. The procedure is illustrated by numerical simulations performed with the *interFoam* solver

from the open source CFD library OpenFOAM, which implements the CF-VOF method. This code is widely used and has recently been applied to study droplet impact in aerosol jet printing (Feng, 2017) and in inkjet printing (Mallinson et al., 2018).

In the remainder of this paper, we present the governing equations, introduce the numerical method and evaluate the effectiveness of different measures proposed in literature for reducing spurious currents on a sessile, a spreading and a receding drop. As main novelty, a new method to suppress artificial equilibrium states arising from the interaction between dynamic contact angle models and spurious currents is proposed and validated for droplet wetting simulations.

2 Simulation methodology

In this section we present the governing equations for the two phase flow, followed by a description of the numerical implementation of surface tension forces and common measures to reduce spurious currents. We then focus on the implementation of contact angle boundary conditions and propose our new method for minimising the influence of spurious currents.

2.1 Governing equations

In the present CF-VOF computations, the two phase flow is described by the volume averaged conservation equations for mass and momentum. For two incompressible, immiscible fluids without slip between the two phases and without phase change these take the form

$$\frac{\partial \alpha}{\partial t} + \nabla \cdot \alpha \mathbf{u} = 0, \tag{1}$$

$$\nabla \cdot \mathbf{u} = 0 \tag{2}$$

for mass conservation and

$$\begin{aligned} &\frac{\partial \rho_\mathrm{m} \mathbf{u}}{\partial t} + \nabla \cdot (\rho_\mathrm{m} \mathbf{u} \otimes \mathbf{u}) \\ &\quad = -\nabla p + \rho_\mathrm{m} \mathbf{g} + \mathbf{f}_\mathrm{c} + \nabla \cdot \mu_\mathrm{m} \left(\nabla \mathbf{u} + (\nabla \mathbf{u})^\mathrm{T} \right) \end{aligned} \tag{3}$$

for the momentum balance (Wörner, 2012). Here, α represents the volume fraction of the liquid phases inside the mesh cell. $1-\alpha$ therefore represents the volume fraction of the gas phase. The volume averaged fluid properties are calculated by $\rho_\mathrm{m} = \alpha\rho_1 + (1-\alpha)\rho_2$ and $\mu_\mathrm{m} = \alpha\mu_1 + (1-\alpha)\mu_2$, where the properties of liquid and gas phases are denoted with indices 1 and 2 respectively. Furthermore, $\mathbf{u}$ denotes the centre-of-mass velocity of the two phases, p the common pressure field and $\mathbf{g}$ the gravity vector.

Assuming that Marangoni stresses are negligible and employing the continuum-surface-force (CSF) method introduced by Brackbill et al. (1992), the capillary forces are given as

$$\mathbf{f}_\mathrm{c} = -\sigma\kappa\delta_\mathrm{b}\mathbf{n}_1, \tag{4}$$

where κ is the interface curvature and $\mathbf{n}_1$ the interface normal vector pointing outward of phase 1. The regularised delta function δ_b allows the capillary forces to be represented by a body force (therefore the subscript b) near the interface. The interface normal $\mathbf{n}_1$ is evaluated from the phase distribution as

$$\mathbf{n}_1 = -\frac{\nabla\alpha}{|\nabla\alpha|} \tag{5}$$

while the interface curvature is given by

$$\kappa = \nabla \cdot \mathbf{n}_1 \tag{6}$$

As regularised delta function the standard version of *interFoam* employs

$$\delta_\mathrm{b} = |\nabla\alpha|. \tag{7}$$

2.2 Numerical implementation

The above equations are discretised using the finite volume method on a collocated grid. To counteract numerical diffusion, an artificial compression term is added to the advection equation of the indicator function. Equation (1) in discrete form then reads

$$\frac{\partial \alpha}{\partial t} + \sum_f \frac{1}{V_i} \left(\langle\alpha\rangle_f \, \phi_f + \langle\alpha\rangle_f \, \langle 1-\alpha \rangle_f \, \phi_\mathrm{cf} \right) = 0, \tag{8}$$

where index f denotes the faces of cell i with volume V_i, and $\phi_f = \langle\mathbf{u}\rangle_f \cdot \mathbf{n}_f S_f$ is the volumetric flux across cell face f with area S_f and outward face normal $\mathbf{n}_f$. $\langle\cdot\rangle_f$ indicates evaluation of the field at cell face f. The compressive flux ϕ_cf is calculated from

$$\phi_\mathrm{cf} = -|\phi| \, \langle\mathbf{n}_1\rangle_f \cdot \mathbf{n}_f \tag{9}$$

(cf. Raeini et al., 2012). The temporal evolution of the α field is obtained from the solution of equation (8) using the multidimensional universal limiter with explicit solution (MULES) algorithm which guarantees boundedness of the solution (OpenFOAM, 2009; Deshpande et al., 2012).

As already described, the interface curvature is obtained from the volume fraction field α. To improve the interface curvature calculation, smoothing the volume fraction field is a common approach (Lafaurie et al., 1994; Brackbill et al., 1992; Aleinov and Puckett, 1995; Kothe et al., 1996). For the calculation of interface curvature we implemented the smoothing procedure introduced by Raeini et al. (2012). A smoothed volume fraction field α_sm is obtained from recursive linear interpolation of cell centred values to the cell faces and interpolating back to the cell centres by calculating the face area weighted average, denoted by $\langle\cdot\rangle_{\mathrm{c}\to\mathrm{f}}$ and $\langle\cdot\rangle_{\mathrm{f}\to\mathrm{c}}$ respectively, for each cell:

$$\alpha_{\mathrm{sm},i} = C_\kappa \langle\langle\alpha_{\mathrm{sm},i-1}\rangle_{\mathrm{c}\to\mathrm{f}}\rangle_{\mathrm{f}\to\mathrm{c}} + (1-C_\kappa)\alpha_{\mathrm{sm},i-1}, \tag{10}$$

where $i = 1, ..., N_\kappa$ and $\alpha_{\mathrm{sm},0} = \alpha$. After $N_\kappa = 2$ iterations with $C_\kappa = 0.5$, the interface curvature is then calculated analogous to equations (5) and (6) using the smoothed volume fraction field $\alpha_\mathrm{sm} = \alpha_{\mathrm{sm},2}$.

Since the regularised delta function is approximated by the gradient of the colour function in equation (7), a smeared colour function implies that the capillary forces act in regions where no interface is present. To address this issue Raeini et al. (2012) proposed a sharpening for the colour function and found that applying the capillary forces in a more narrow region within the smeared interface reduces spurious currents significantly. Here, the heuristic sharpening coefficient in the method of Raeini et al. (2012) is set to 0.5, so that the sharpened volume fraction field is given by

$$\alpha_{\mathrm{sh}} = \begin{cases} 0 & \text{for } \alpha < \frac{1}{4} \\ 2\alpha - \frac{1}{2} & \text{for } \frac{1}{4} \leq \alpha < \frac{3}{4} \\ 1 & \text{for } \alpha \geq \frac{3}{4} \end{cases} \tag{11}$$

The regularised delta function δ_{b} is then calculated as $\delta_{\mathrm{b}} = |\nabla \alpha_{\mathrm{sh}}|$.

2.3 Contact angle boundary condition

The wetting properties at the three phase contact line are accounted for by a boundary condition for $\mathbf{n}_1$. Along the substrate boundary of the fluid domain Γ_{w} the interface normal vector is corrected by

$$\mathbf{n}_1^*|_{\Gamma_{\mathrm{w}}} = \mathbf{n}_{\mathrm{w}} \cos(\theta) + \frac{\mathbf{n}_1 - (\mathbf{n}_1 \cdot \mathbf{n}_{\mathrm{w}})\,\mathbf{n}_{\mathrm{w}}}{|\mathbf{n}_1 - (\mathbf{n}_1 \cdot \mathbf{n}_{\mathrm{w}})\,\mathbf{n}_{\mathrm{w}}|} \sin(\theta) \tag{12}$$

to impose the apparent contact angle θ (Berberović, 2010; Deshpande et al., 2012). Here, $\mathbf{n}_{\mathrm{w}}$ is the outward unit normal vector of the solid substrate. Within the fluid domain Ω the interface normal vector remains unchanged ($\mathbf{n}_1^*|_{\Omega} = \mathbf{n}_1$). The interface normal vector $\mathbf{n}_1^*$ corrected in that way is then used in equation (6) to calculate the interface curvature. The contact angle boundary condition gives, therefore, rise to additional surface tension forces forcing the wetting line towards a state with the prescribed contact angle. These forces act as long as the phase distribution near the substrate differs from the prescribed contact angle. Note that θ does not have to be constant for the whole substrate but can be a function of further variables, e.g., Ca, as is the case in many dynamic contact angle models including that of Kistler.

2.4 Dynamic contact angle modelling

In the present paper we adopt the dynamic contact angle model of Kistler (1993). This is a semi-heuristic model based on experimental data by Hoffman (1975) where the dynamic contact angle is given by

$$\theta_{\mathrm{d}} = f_{\mathrm{Hoff}}\left[Ca + f_{\mathrm{Hoff}}^{-1}(\theta_{\mathrm{e}})\right] \tag{13}$$

with

$$f_{\mathrm{Hoff}}(x) = \cos^{-1}\left\{1 - 2\tanh\left[5.16\left(\frac{x}{1+1.31x^{0.99}}\right)^{0.706}\right]\right\}. \tag{14}$$

This model has been used in several numerical studies on impinging and spreading droplets, e.g., Šikalo et al. (2005) and Roisman et al. (2008).

For small capillary numbers and complete wetting situations ($\theta_{\mathrm{e}} = 0°$), the Kistler model approximates the Tanner law. However, the application of the Kistler model is not restricted to small capillary numbers and complete wetting situations. Furthermore, for negligible inertial forces in the inner region close to the contact line, equation (13) can also be applied to receding contact lines, i.e., $Ca < 0$ (Šikalo et al., 2005). Because f_{Hoff} is not defined for a negative argument, however, special care has to be taken for $Ca + f_{\mathrm{Hoff}}^{-1}(\theta_{\mathrm{e}}) < 0$. Eggers (2005) showed for small equilibrium contact angles, where lubrication theory can be applied, that at a critical capillary number $Ca_{\mathrm{cr}} < 0$ corresponding to $\theta_{\mathrm{d}} = 0$ the contact line disappears. For $Ca < Ca_{\mathrm{cr}}$ a thin film is deposited (Eggers, 2005), as previously described by Landau and Levich (1942) and Derjaguin (1943) and more recently experimentally also observed, for example, by Delon et al. (2008). To include the deposition of a thin film for receding contact lines we therefore employed

$$\theta_{\mathrm{d}} = \begin{cases} 0 & \text{for } Ca < Ca_{\mathrm{cr}} \\ f_{\mathrm{Hoff}}\left[Ca + f_{\mathrm{Hoff}}^{-1}(\theta_{\mathrm{e}})\right] & \text{for } Ca \geq Ca_{\mathrm{cr}} \end{cases} \tag{15}$$

as dynamic contact angle model throughout the present work, with $Ca_{\mathrm{cr}} = -f_{\mathrm{Hoff}}^{-1}(\theta_{\mathrm{e}})$ corresponding to $\theta_{\mathrm{d}} = 0$ according to equation (13). Note that this model does not explicitly account for contact angle hysteresis. However, for the small inertial forces present in the cases considered within this work, overshooting spreading (receding) beyond the advancing (receding) contact angle is not expected. Hysteresis could therefore simply be considered by setting θ_{e} to the advancing or receding contact angle respectively.

Figure 1 shows the branch $Ca \geq Ca_{\mathrm{cr}}$ of equation (15) for three different equilibrium contact angles. For small absolute values of Ca, a large gradient of θ_{d} can be observed. This indicates the large sensitivity of the Kistler model and similar models to inaccurate estimation of the contact line speed u_{cl} for systems with very good wettability. As θ_{e} increases, this sensitivity is reduced for $Ca \geq 0$.

For implementation of dynamic contact angle models such as that of Kistler, Ca has to be evaluated on the boundary faces of the solid surface. As discussed in the introduction, there is no general consensus how the contact line velocity u_{cl} should be approximated especially for methods with non-sharp interface representation. In the present study we follow Berberović (2010) and calculate u_{cl} by projecting the velocity in the cell centres immediately adjacent to the substrate $\mathbf{u}_P$ onto the contact line normal vector tangential to the substrate

$$u_{\mathrm{cl}} = \frac{\mathbf{n}_1 - (\mathbf{n}_1 \cdot \mathbf{n}_{\mathrm{w}})\,\mathbf{n}_{\mathrm{w}}}{|\mathbf{n}_1 - (\mathbf{n}_1 \cdot \mathbf{n}_{\mathrm{w}})\,\mathbf{n}_{\mathrm{w}}|} \cdot \mathbf{u}_P. \tag{16}$$

Considering the fact that $\mathbf{u}_P$ is the velocity which is used to advect the volume fraction, this is a natural choice. However, we would like to note that this approach is

only reasonable when there exists slip in the numerical simulation.

Figure 1 Dependence of dynamic contact angle on capillary number in the Kistler model for equilibrium contact angles 0°, 12° and 20° (see online version for colours)

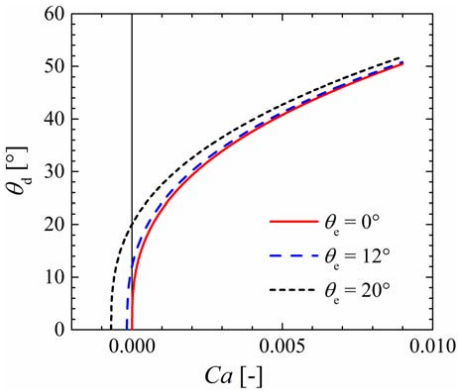

For the simulation results to be presented in Subsections 3.3 and 3.4, Ca is determined using the approximation of u_{cl} given in equation (16). The dynamic contact angles calculated from equation (15) are then used to correct the interface normal vectors along the substrate boundary using equation (12). By that means, a different contact angle is calculated in each time step and for every cell face coinciding with the substrate boundary. The resulting interface normal vector then enters into the calculation of interface curvature and surface tension forces.

2.5 *Proposed method for suppressing artificial equilibrium states in spreading simulations*

As will be shown in Section 3, spreading simulations employing a dynamic contact angle model may produce artificial equilibrium states in the presence of spurious currents. In order to suppress such artificial equilibrium states, we introduce an additional step in the evaluation of the contact line velocities. Similar to the calculation of interface curvature from a smoothed indicator function described above, we introduce a smoothing step for the velocity field. Analogous to the smoothing procedure for α_{sm} by Raeini et al. (2012), the velocity field is smoothed by recursive linear interpolation of the cell-centred values to the face centres and interpolating back to the cell centres by calculating the cell area weighted average for each cell

$$\mathbf{u}_{\mathrm{sm},i} = C_{\mathbf{u}} \langle \langle \mathbf{u}_{\mathrm{sm},i-1} \rangle_{\mathrm{c}\to\mathrm{f}} \rangle_{\mathrm{f}\to\mathrm{c}} + (1 - C_{\mathbf{u}}) \mathbf{u}_{\mathrm{sm},i-1}, \qquad (17)$$

where $i = 1, ..., N_{\mathbf{u}}$ and $\mathbf{u}_{\mathrm{sm},0} = \mathbf{u}$. This smoothing procedure is not limited to cells adjacent to the substrate boundary, but takes also velocities further within the domain into account.

The number of iterations $N_{\mathbf{u}}$ for equation (17) determine in combination with the choice of $C_{\mathbf{u}}$ the intensity of the smoothing. The size of the smoothing region is defined by the number of iterations. It increases by one cell with every iteration. Therefore the radius of spurious vortices can be used as a reference for the number of iterations while the relaxation parameter $C_{\mathbf{u}}$ allows to set the smoothing intensity independently. This allows to find a better compromise between damping of spurious currents and a sufficiently detailed representation of the velocity field. Numerical experiments showed that for the considered flows in the present study two iterations were sufficient while deactivating the relaxation by setting $C_{\mathbf{u}} = 1$ yielded the best results. This number of iterations agrees well with the diameter of the dominant spurious vortex at the contact line in Figure 6 of approximately five grid spacings. Figure 2 illustrates the smoothing procedure by interpolation within a single iteration of equation (17). The schematic diagram shows how local inhomogeneities are already significantly reduced after one iteration while the overall flow direction and magnitude are largely preserved. Note that this modified velocity field is only used for the evaluation of the dynamic contact angles while the unaltered field is used in the mass and momentum balance equations.

Figure 2 Sketch of the smoothing procedure for an arbitrary cell-centred velocity field, (a) initial state (b) after interpolation to the cell faces (c) after interpolation back to the cell centres (see online version for colours)

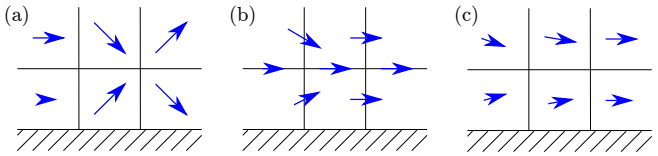

Another aspect that needs to be considered in this context is the numerical smearing of the interface in methods such as CF-VOF. As the interface is smeared out over a certain volume, the three phase contact line becomes a ‘three-phase contact area’. For small contact angles this area is particularly large. Therefore, surface tension forces will be applied in several cells along the substrate and normal to the contact line. If a dynamic contact angle model is used, the interface normal vectors will be corrected based on the local velocity in each cell. Since velocities in neighbouring cells in general differ, each face will have a different normal vector. This will then lead to a curvature within the ‘three-phase contact area’. The extension of the contact line to an area already needs to be considered unphysical from a macroscopic viewpoint. Therefore, this curvature must be a numerical artefact. Since the additional curvature leads to surface tension forces that will potentially induce spurious currents, the interface normal vectors along the substrate will be smoothed in an additional step.

Raeini et al. (2012) observed a related effect when using a static contact angle on castellated boundaries. Based on the work of Huang et al. (2005) they smoothed the wall normal vectors $\mathbf{n}_{\mathrm{S}}$ by interpolating five times from face centres to vertices and back to the centres. We adopted their method in order to smooth the interface normal vectors $\mathbf{n}_1^*|_{\Gamma_{\mathrm{w}}}$ along the substrate boundary calculated

from equations (12), (14), (15) and (16). The smoothing procedure in general reads

$$\mathbf{n}_1^*|_{\Gamma_\mathrm{w},i} = C_\mathbf{n}\langle\langle \mathbf{n}_1^*|_{\Gamma_\mathrm{w},i-1}\rangle_{\mathrm{f}\to\mathrm{v}}\rangle_{\mathrm{v}\to\mathrm{f}} + (1-C_\mathbf{n})\mathbf{n}_1^*|_{\Gamma_\mathrm{w},i-1}, \quad (18)$$

where $i = 1, ..., N_\mathbf{n}$ and $\mathbf{n}_1^*|_{\Gamma_\mathrm{w},0} = \mathbf{n}_1^*|_{\Gamma_\mathrm{w}}$. As opposed to the smoothing procedure for the velocity field, only interface normal vectors on the boundary faces are hereby taken into account. After the last iteration, each normal vector is normalised to unity. We again found best results without relaxation by choosing $C_\mathbf{n} = 1$. Following Raeini et al. (2012), $N_\mathbf{n} = 5$ smoothing iterations are conducted before $\mathbf{n}_1^*|_{\Gamma_\mathrm{w},5}$ is used in equation (6) to calculate the interface curvature.

2.6 Description of droplet test cases

For validation of the new method presented in Subsection 2.5, an initially hemispherical droplet with volume 6 pL is considered. Accordingly, the initial wetting radius and drop height are 14.2 µm. Both, the liquid within the droplet and the surrounding gas are initially at rest. The physical properties of both phases are listed in Table 1. These and the drop volume are typical for applications in inkjet printing.

Table 1 Physical properties of the phases

		Liquid	*Gas*
ρ	$\mathrm{kg\,m^{-3}}$	1,050	1.204
μ	mPa s	20	19.01e-3
σ	$\mathrm{mN\,m^{-1}}$	23	

Figure 3 Computational domain with initial conditions

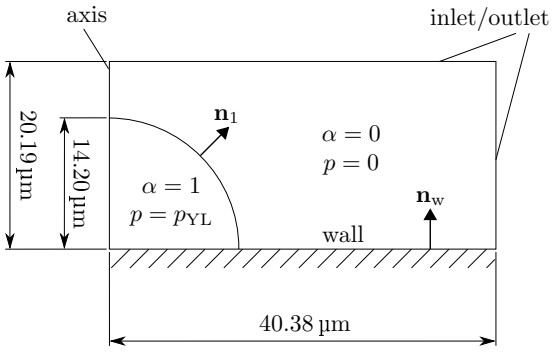

We take advantage of the rotational symmetry of the problem and perform 2D axisymmetric simulations. Figure 3 shows a sketch of the computational domain including the initial conditions for α and the pressure field with $p_\mathrm{YL} = 2\sigma/R \approx 3.2$ kPa. Along the substrate the normal pressure gradient was set to zero and a no slip and no penetration condition was used. For the volume fraction a contact angle boundary condition as described above was employed. At the lateral and top boundaries of the computational domain a fixed value of $p = 0$ Pa was set while a zero gradient condition was used for the velocity field. The boundary condition for the volume fraction changes based on the flow direction between a zero gradient condition for an outflow and a fixed value of zero for an inflow. The wedge shaped mesh consists of one cell in angular direction and 105×120 cells in axial and radial directions. Grading was used to increase the mesh resolution towards the axis and towards the substrate resulting in mesh widths between 0.09 µm and 0.47 µm.

In order to integrate the system of partial differential equations in time, a suitable choice for the time step size (Δt) has to be made. The explicit solution procedure for the α advection equation hereby imposes a limitation. When developing the CSF method, Brackbill, Kothe and Zemach (BKZ) (1992) also introduced a criterion for the time step size. It takes the propagation of capillary waves into account and reads

$$\Delta t_\mathrm{BKZ} < \sqrt{\frac{(\rho_1+\rho_2)h^3}{4\pi\sigma}} \quad (19)$$

with h denoting the mesh spacing. This criterion can pose a severe restriction as h decreases with increasing grid resolution. As Galusinski and Vigneaux (2008) pointed out, it neglects, however, the stabilising effect of viscous damping. Deshpande, Anumolu and Trujilo (DAT) (2012) numerically evaluated the criterion of Galusinski and Vigneaux (2008) for *interFoam* under the restriction of matched density and viscosity of both phases. From in total 80 test simulations, they proposed the criterion

$$\Delta t_\mathrm{DAT} \leq \max\left(10\,\frac{\mu h}{\sigma},\quad 0.1\sqrt{\frac{\rho h^3}{\sigma}}\right) \quad (20)$$

which poses a weaker restriction on Δt on fine grids as compared to equation (19). In the present simulations, equation (20) is evaluated in the vicinity of the interface using ρ_m and μ_m and the time step size is dynamically adjusted accordingly.

The computational domain, initial and boundary conditions, mesh and time step criteria described so far are the same for the first three test cases considered in this paper. What differs is the value of the equilibrium contact angle and whether a constant or dynamic contact angle model is used. For the receding droplet test cases the initial conditions for the phase distribution and the pressure field are varied additionally.

3 Results

In this section, we first evaluate the effect of the smoothing and sharpening steps presented in Subsection 2.2 on spurious currents on a sessile drop with a constant contact angle model. Next, the effects of these measures on the spreading behaviour and equilibrium state are discussed. Subsequently, the proposed smoothing procedures for contact line velocity and interface normal vectors are applied to a spreading and a receding droplet with Kistler dynamic contact angle model and the results are compared to a simulation without these additional measures.

3.1 *Spurious currents for a sessile droplet*

To validate the effects of the smoothing and sharpening steps for the volume fraction field (α) on spurious currents we evaluate the velocities arising in the simulation of a hemispherical sessile droplet. For this purpose, we neglect gravity and set $\theta_e = 90°$. With both phases being initially at rest, the velocity field within the droplet as well as in the surrounding gas phase should ideally remain zero. Therefore, all developing currents have to be considered spurious.

Figure 4 Different methods to reduce spurious currents compared to the standard *interFoam*-implementation (see online version for colours)

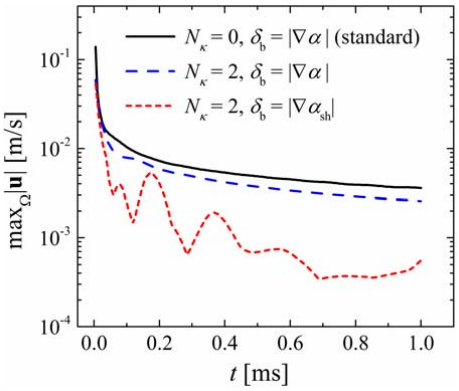

In Figure 4, the maximal velocity magnitude within the computational domain is plotted over time for the different surface tension formulations. While calculating the interface curvature on a smoothed α field decreases the magnitude of spurious currents by approximately 30%, an even better result is achieved when capillary forces are applied in a narrowed region within the smeared interface. For the present test case, this reduces spurious currents by almost one order of magnitude. This trend agrees with the findings of Raeini et al. (2012) and more recently by Aboukhedr et al. (2018), even though the positive effects of smoothing and sharpening are not as pronounced here as for the relaxing bubble test case in the original work.

3.2 *Spreading droplet with constant contact angle*

As second test case, we apply the two above methods for calculating surface tension forces from a smoothed α field to a spreading droplet. Mesh and initial conditions remain unchanged but now the equilibrium contact angle $\theta_e = 12°$ is prescribed at the substrate boundary.

In Figure 5, the computed contact line diameters are plotted over time. For negligible gravitational forces the equilibrium shape of the droplet is a spherical cap. The equilibrium contact line diameter can then be calculated from θ_e and the drop volume (Strella, 1970). The corresponding value of 66.17 µm is indicated by the dash-dotted horizontal line. Figure 5 shows that for the sharpened δ-function the droplet does not reach the correct equilibrium state as the terminal contact line diameter is substantially underestimated. On the other hand, for a smoothed α field without sharpening of the δ-function the contact line diameter increases continuously and approaches the correct equilibrium state asymptotically.

Figure 5 Time evolution of wetted diameter in spreading simulation with constant contact angle ($\theta_e = 12°$) (see online version for colours)

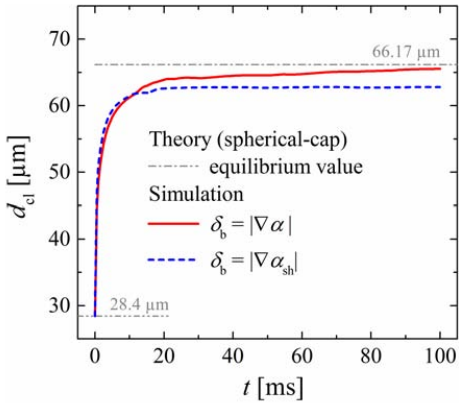

Note: Both simulations employ smoothed curvature computation but use different formulations for the delta function.

Table 2 Capillary pressure jump computed with different contact angle models at $t = 100$ ms

Contact angle model		Δp_c / *Pa*	*rel. error* / %
Constant	$N_\kappa = 2$, $\delta_b = \lvert\nabla\alpha\rvert$	293.51	1.53
	$N_\kappa = 2$, $\delta_b = \lvert\nabla\alpha_{sh}\rvert$	354.99	22.80
Dynamic	$N_\kappa = 2$, $\delta_b = \lvert\nabla\alpha\rvert$	1,481.36	412.42
	$N_\kappa = 2$, $N_\mathbf{n} = 5$, $N_\mathbf{u} = 2$, $\delta_b = \lvert\nabla\alpha\rvert$	282.91	2.14

In Table 2, the capillary pressure is listed for both simulations at $t = 100$ ms. According to the lower terminal contact line diameter, the pressure within the droplet modelled with the sharpened δ-function is overestimated. Though this method significantly reduces spurious currents, it is thus unsuitable for simulations of systems with good wetting properties (low values of θ_e) close to their equilibrium states.

3.3 *Spreading droplet with dynamic contact angle*

So far we have considered simulations with constant (equilibrium) contact angle to validate the measures described in Subsection 2.2 for reducing spurious currents for sessile and spreading droplets. In this subsection, we present results of spreading simulations obtained with the dynamic contact angle boundary condition at the substrate using the Kistler model from equation (15) with equilibrium contact angle $\theta_e = 12°$. In contrast to the two former test cases, we account for gravitational forces by setting $\mathbf{g} = -g\,\mathbf{n}_w$ where $g = 9.81\ \mathrm{m\,s^{-2}}$. Their influence is, however, very small as the Bond number $Bo = \rho g R^2/\sigma =$ 9.04e-5 is much smaller than unity.

3.3.1 *Standard method for evaluation of* u_{cl}

First we consider the case where the contact line velocity is evaluated directly from the bulk velocity field according to equation (16). Using this approach, the droplet ceases to spread after only a few milliseconds. The terminal droplet shape and velocity field are depicted in Figure 6. Though the droplet shape (solid line) has not reached the spherical cap shape corresponding to $\theta_{\mathrm{e}} = 12°$ (dotted line), the droplet does not continue to spread. Since the computed steady droplet shape differs significantly from the theoretical equilibrium state, the computed equilibrium state has to be considered artificial.

Figure 6 Droplet shape (solid line) and velocity field for simulation with $\theta_{\mathrm{e}} = 12°$ employing the Kistler dynamic contact angle model after 100 ms of spreading (see online version for colours)

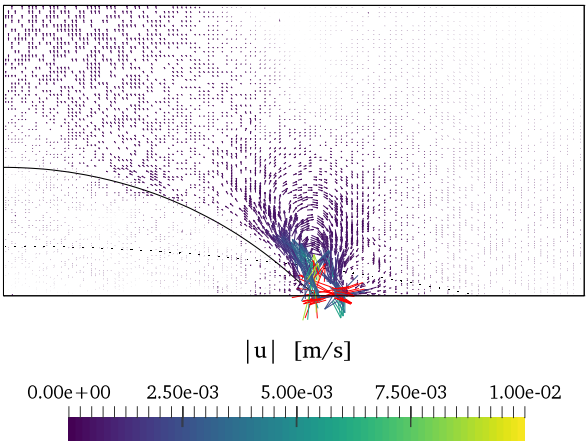

Notes: Velocities exceeding 1e-2 $\mathrm{m\,s^{-1}}$ are displayed in red. The dotted line indicates the theoretical equilibrium shape corresponding to a spherical cap.

The cause for this artificial equilibrium state is the spurious vortex in the vicinity of the three phase contact line visible in Figure 6. In fact, the magnitude of spurious velocities at the contact line has increased significantly compared to the results in Subsection 3.1. Furthermore, the location of the maximum spurious velocities has shifted from an interface position within the fluid domain towards the contact line at the wall, indicating a coupling between spurious currents and the dynamic contact angle model. At the contact line, the spurious velocities with magnitude up to $0.183\ \mathrm{m\,s^{-1}}$ lead to the estimated u_{cl} oscillating between approximately $\pm 0.17\ \mathrm{m\,s^{-1}}$ corresponding to a capillary number $Ca = \pm 0.148$. By equation (15) these values of Ca correspond to a dynamic contact angle of $\theta_{\mathrm{d}} = 130.87°$ or $\theta_{\mathrm{d}} = 0°$ respectively. This oscillation of the dynamic contact angle leads to oscillating capillary forces at the contact line which then in turn lead to an oscillating contact line velocity. In conclusion, the finite magnitude of the spurious currents results in finite values $u_{\mathrm{cl}} \neq 0$ and $Ca \neq 0$ so that the limits $Ca \to 0$ and $\theta_{\mathrm{d}} \to \theta_{\mathrm{e}}$ corresponding to the correct physical equilibrium states can never be reached. Instead, the spreading stops earlier resulting in an artificial equilibrium shape of the drop whose state is actually depending on the magnitude of the spurious currents in combination with the implemented dynamic contact angle model.

Since the droplet shape is in such poor agreement with the theoretical equilibrium state, the capillary pressure, which is listed in Table 2, is significantly overestimated compared to the theoretical value $\Delta p_{\mathrm{c}} = 2\sigma/R \approx 289.09$ Pa. This can be expected to falsify macroscopic flow properties on more complex geometries, such as, e.g., the rise height in a capillary. The coupling with spurious currents therefore can significantly impair the predicitve capabilities of simulations with dynamic contact angle models for smaller capillary numbers unless further measures are introduced.

3.3.2 *Improved method for evaluation of* u_{cl}

Figure 7 shows the equilibrium state from an otherwise identical simulation where the interface curvature is evaluated based on the method introduced in Subsection 2.5. The terminal droplet shape is now in excellent agreement with the expected spherical cap shape. Moreover, the maximum magnitude of spurious velocities in the whole computational domain has decreased by more than one order in magnitude. According to the good agreement of the droplet shape with the theoretical equilibrium state also the capillary pressure in Table 2 agrees quite well with the theoretical value calculated from the Young-Laplace equation.

We showed that the additional smoothing procedures can help to improve the predicted equilibrium states in simulations with dynamic contact angle models. The motivation to use dynamic contact angle models in the first place was, however, to better capture the spreading dynamics and the transition towards low capillary numbers. For that reason we considered the temporal evolution of the contact line diameter for three different contact angle implementations. Figure 8 shows a double-logarithmic plot of the contact line diameters over time. The results of the simulations discussed above are compared to the simulation from Subsection 3.2 with a constant contact angle and without sharpened surface force. As discussed earlier, for a dynamic contact angle model with the contact line velocity directly evaluated from velocities in adjacent cells, the equilibrium contact line radius is underestimated. Applying the additional smoothing allows the droplet to continue spreading towards its physical equilibrium state. Yet, for earlier stages of the spreading process the smoothing procedure does not negatively effect the dynamics.

Figure 8 shows that the wetted diameter scales as $d_{\mathrm{cl}} \sim t^{0.127}$ in the time interval 0.2–10 ms. The spreading dynamics in this period thus agrees reasonable well with Tanner's law, where the exponent of the power law is 0.1. Since the Kistler model approximates the relation $\theta_{\mathrm{d}} \propto \sqrt[3]{Ca}$ for small Ca, this behaviour is expected. Interestingly, even with a constant contact angle the contact line diameter seems to follow Tanner's law. Boelens and de Pablo (2019) very recently found similar results with a generalised Navier slip boundary condition included in the algebraic

VOF model, when the slip length is resolved by the grid resolution. With the numerical slip present in our simulation, the double-logarithmic plots for a constant contact angle and a smoothed dynamic contact angle are nearly parallel over a period of a few milliseconds, with the static contact angle leading to faster spreading.

Figure 7 Velocity field in quasi steady state with Kistler dynamic contact angle model ($\theta_e = 12°$) (see online version for colours)

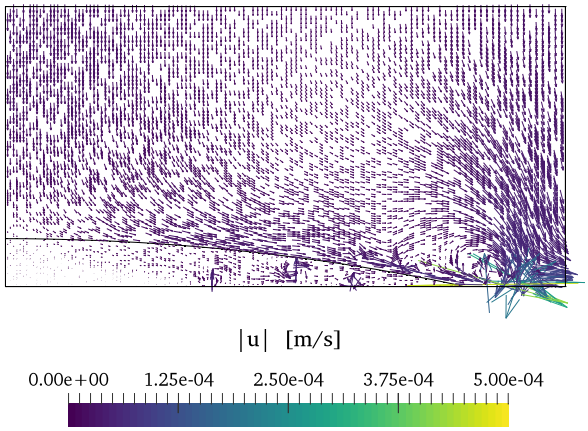

Notes: The droplet contour (solid line) coincides with the spherical cap contour (displayed as dotted line in Figure 6). Note the reduced range of the colour map compared to Figure 6. The arrows were rescaled accordingly.

Figure 8 Effect of the smoothed velocity and interface normal vector fields in conjunction with the Kistler contact angle model on the spreading dynamics (see online version for colours)

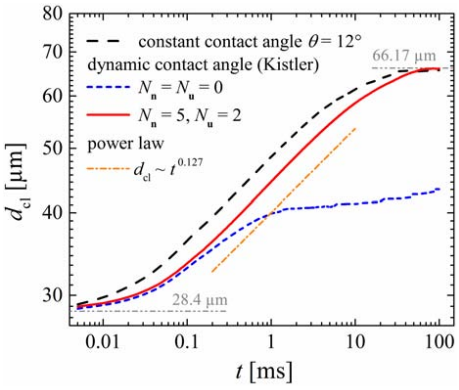

An explanation for the agreement with Tanner's law even without specification of a dynamic contact angle can be found if one compares the numerical implementation of contact angle boundaries to the derivation of Tanner's law. Assuming the presence of a thin layer of liquid similar to a precursor film in front of the macroscopic contact line, the macroscopic contact angle can be found from the mass and momentum balances for a Stokes flow in the micro region in the vicinity of the contact line (Tanner, 1979). The viscous forces for a given contact line velocity and the related pressure gradient are balanced by capillary forces and, therefore, the slope in the micro region depends on the spreading velocity. This leads to the well-known proportionality between the dynamic contact angle and the capillary number (Tanner, 1979).

Since the contact angle boundary condition was introduced through a correction of the interface normal vectors $\mathbf{n}_1$, the numerical model is closely related to Tanner's reasoning for the contact line dynamics. By correcting $\mathbf{n}_1$ at the substrate boundary, a kink in the field of interface normal vectors is introduced at the contact line. This leads to additional surface tension forces in the contact line region. If gravitational and inertial forces are negligible, these capillary forces will be counteracted mainly by viscous friction in the contact line region. Furthermore, for a static contact angle of 0° the interface normal vectors are corrected to be perpendicular to the substrate. This orientation of the interface normal vectors could also be interpreted as a sub-grid scale precursor film. The characteristic length scale for the numerical static contact angle model however is mesh dependent because the kink in interface normal vectors always appears between the boundary face and the adjacent cell centre value. Furthermore, without introducing a slip model, the slip length is also mesh dependent. Boelens and de Pablo (2019) showed that introducing a generalised Navier slip model is a possible remedy that can reproduce spreading according to Tanner's law. However, this requires the slip length to be resolved by the grid. With sufficient (numerical) slip present, the use of a dynamic contact angle is an alternative that allows the use of coarser meshes while still correctly capturing the contact line dynamics.

In order to demonstrate the proposed method's ability to correctly capture the spreading dynamics over a range of capillary numbers, we evaluated the apparent dynamic contact angles and corresponding capillary numbers from each droplet spreading simulation presented in Figure 8. The contact angle was therefore evaluated from the droplet contour and the contact line velocity from the temporal change of the wetted diameter. Because the initial condition of a hemispherical static droplet is not in accordance with the employed contact angle models, we excluded the data of the first 4 µs. Figure 9 shows the results of the spreading simulation in comparison with the Kistler model [equation (13)] for an equilibrium contact angle of 12°. Both, the spreading results obtained with a constant contact angle model as well as with the Kistler contact angle model in conjunction with the proposed smoothing method predict the expected equilibrium contact angle of 12°. The results obtained from the simulation with Kistler model without additional smoothing of the velocity field and interface normals again show a large deviation from the expected static state. While the contact angle data at larger Ca_{cl} for both simulations with dynamic contact angle model agree reasonably well with the Kistler model, the additional smoothing method also allows to capture the contact line dynamics at lower capillary numbers. As expected, the apparent contact angle data from the spreading simulation with a constant contact angle model deviates from the contact line dynamics predicted by the Kistler model,

indicating the importance of an adequate dynamic contact angle model.

Figure 9 Apparent contact angle data and corresponding capillary numbers evaluated from the droplet spreading simulations presented in Figure 8 in comparison with the Kistler model for $\theta_e = 12°$ (see online version for colours)

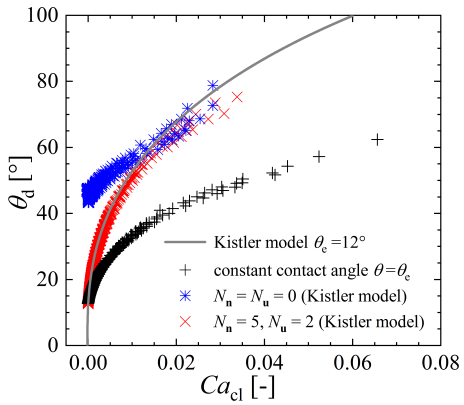

3.4 Receding droplet with dynamic contact angle

For droplet impingement at higher Weber numbers or for larger equilibrium contact angles, droplets might spread beyond their equilibrium state and reach their equilibrium with a receding contact line. In order to verify the smoothing procedure proposed above for this case, we considered the following problem: a droplet of volume 6 pL is receding from an initial spherical cap shape with a contact angle of 12° towards its equilibrium state with a prescribed contact angle of 90°. The initial condition for the phase distribution is set accordingly. The initial pressure jump across the liquid-gas interface is $p_{YL} \approx 289.09$ Pa. Apart from these changes the set-up is identical to the previous test case.

Figure 10 compares the results of the receding droplet test case for:

1 a constant contact angle model

2 the Kistler model with the standard method for evaluation of u_{cl} from the bulk velocity according to equation (16)

3 the Kistler model in conjunction with the method for evaluation of u_{cl} and interface normals as proposed in Subsection 2.5.

Just as in the spreading droplet scenario, employing a dynamic contact angle model without additional measures leads to premature and artificial pinning of the contact line. With the proposed smoothing procedure during the evaluation of u_{cl} and interface normals, however, the droplet continues to recede towards its expected equilibrium state. Furthermore, as the comparison to the constant contact angle model shows, the slowing of the contact line as described by the Kistler model can be maintained with the additional smoothing steps. This final test case therefore demonstrates the relevance of both, dynamic contact angle modelling as well as a suitable evaluation method for the contact line velocity and interface normals for dewetting scenarios at low capillary numbers and verifies the method proposed in Subsection 2.5 also for the dewetting case.

Figure 10 Effect of the smoothed velocity and interface normal vector fields in conjunction with the Kistler contact angle model on the dewetting dynamics (see online version for colours)

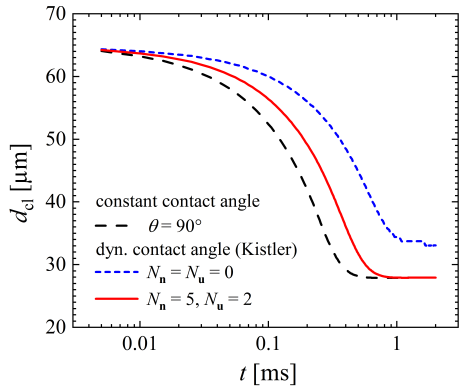

4 Conclusions

In this article we discussed the relevance of dynamic contact angle models for droplet spreading simulations at low capillary numbers. We showed that spurious currents can cause equilibrium states with artificially increased contact angles which lead to errors in other macroscopic properties such as the wetted diameter or the capillary pressure. In a first attempt to suppress these artificial states we calculated the interface curvature on a smoothed volume fraction field and applied surface tension forces using a sharp surface force approach. However, the sharp surface force method itself had negative effects on the equilibrium state while smoothing the volume fraction alone has proven insufficient. We therefore introduced a new method to suppress artificial equilibrium states arising from the interaction between dynamic contact angle models and spurious currents by additional smoothing of velocities and interface normal vectors. We were able to show that this method allows the use of dynamic contact angle models even for low contact line speeds or capillary numbers, capturing the equilibrium state correctly, while leaving the spreading dynamics at larger contact line speeds unaffected.

Acknowledgements

This article is based on the master thesis of the first author at the Mechanical Engineering Department of Karlsruhe Institute of Technology (KIT), assigned by Prof. Bettina Frohnapfel (Institute of Fluid Mechanics). Her support is gratefully acknowledged. Furthermore, the first author kindly acknowledges the support by the German Research Foundation (DFG) within the Collaborative Research

Centre 1194 ‘Interaction between Transport and Wetting Processes’ as associated member of the CRC.

References

Aboukhedr, M., Georgoulas, A., Marengo, M., Gavaises, M. and Vogiatzaki, K. (2018) ‘Simulation of micro-flow dynamics at low capillary numbers using adaptive interface compression’, *Computers & Fluids*, Vol. 165, pp.13–32.

Aleinov, I. and Puckett, E.G. (1995) ‘Computing surface tension with high-order kernels’, *Proceedings of the 6th International Symposium on Computational Fluid Dynamics*, Lake Tahoe, CA, pp.4–8.

Berberović, E. (2010) *Investigation of Free-surface Flow Associated with Drop Impact: Numerical Simulations and Theoretical Modeling*, PhD thesis, Technische Universität Darmstadt.

Boelens, A.M. and de Pablo, J.J. (2019) ‘Generalised Navier boundary condition for a volume of fluid approach using a finite-volume method’, *Physics of Fluids*, Vol. 31, No. 2, pp.021203-1–12.

Bonn, D., Eggers, J., Indekeu, J., Meunier, J. and Rolley, E. (2009) ‘Wetting and spreading’, *Reviews of Modern Physics*, Vol. 81, No. 2, pp.739–805.

Brackbill, J.U., Kothe, D.B. and Zemach, C. (1992) ‘A continuum method for modeling surface tension’, *Journal of Computational Physics*, Vol. 100, No. 2, pp.335–354.

Bussmann, M., Mostaghimi, J. and Chandra, S. (1999) ‘On a three-dimensional volume tracking model of droplet impact’, *Physics of Fluids*, Vol. 11, No. 6, pp.1406–1417.

Delon, G., Fermigier, M. Snoeijer, J.H. and Androetti, B. (2008) ‘Relaxation of a dewetting contact line. Part 2. Experiments’, *Journal of Fluid Mechanics*, Vol. 604, pp.55–75.

Derjaguin, B.V. (1943) ‘Thickness of liquid layer adhering to walls of vessels on their emptying and the theory of photo-and motion-picture film coating’, *(Dokl.) Acad. Sci. URSS*, Vol. 39, pp.13–16.

Deshpande, S.S., Anumolu, L. and Trujilo, F. (2012) ‘Evaluating the performance of the two-phase flow solver interFoam’, *Computational Science & Discovery*, Vol. 5, No. 1, pp.014016-1–36.

Dupont, J-B. and Legendre, D. (2010) ‘Numerical simulation of static and sliding drop with contact angle hysteresis’, *Journal of Computational Physics*, Vol. 229, No. 7, pp.2453-–2478.

Eggers, J. (2005) ‘Existence of receding and advancing contact lines’, *Physics of Fluids*, Vol. 17, No. 8, pp.082106-1–10.

Feng, J.Q. (2017) ‘A computational study of high-speed microdroplet impact onto a smooth solid surface’, *Journal of Applied Fluid Mechanics*, Vol. 10, No. 1, pp.243–256.

Galusinski, C. and Vigneaux, P. (2008) ‘On stability condition for bifluid flows with surface tension: application to microfluidics’, *Journal of Computational Physics*, Vol. 227, No. 12, pp.6140–6164.

Hoffman, R.L. (1975) ‘A study of the advancing interface. I. Interface shape in liquid-gas systems’, *Journal of Colloid and Interface Science*, Vol. 50, No. 2, pp.228–241.

Huang, H., Meakin, P. and Liu, M.B. (2005) ‘Computer simulation of two-phase immiscible fluid motion in unsaturated complex fractures using a volume of fluid method’, *Water Resources Research*, Vol. 41, No. 12, pp.W12413-1–12.

Josserand, C. and Thoroddsen, S.T. (2016) ‘Drop impact on a solid surface’, *Annual Review of Fluid Mechanics*, Vol. 48, pp.365–391.

Kistler, S.F. (1993) ‘Hydrodynamics of wetting’, in Berg, J.C. (Ed.): *Wettability*, Marcel Dekker, New York, NY.

Kothe, D.B., Rider, W.J.W., Mosso, S.J., Brock, J.S. and Hochstein, J.I. (1996) ‘Volume tracking of interfaces having surface tension in two and three dimensions’, In *Proceedings of the 34th Aerospace Sciences Meeting & Exhibit*, AIAA Report 96-0859, 15–18 January, Reno, NV.

Landau, L.D. and Levich, B.V. (1942) ‘Dragging of a liquid by a moving plate’, *Acta Physiochim*, Vol. 17, pp.42–54.

Lafaurie, B., Nardonne, C., Scardovelli, R., Zaleski, S. and Zanetti, G. (1994) ‘Modelling merging and fragmentation in multiphase flows with SURFER’, *Journal of Computational Physics*, Vol. 113, No. 1, pp.134–147.

Linder, N., Criscione, A., Roisman, I.V., Marschall, H. and Tropea, C. (2015) ‘3D computation of an incipient motion of a sessile drop on a rigid surface with contact angle hysteresis’, *Theoretical and Computational Fluid Dynamics*, Vol. 29, Nos. 5–6, pp.373–390.

Mallinson, S.G., Barber, T.J., Yeoh, G.H. and McBain, G.D. (2018) ‘Simulation of droplet impact and spreading using a simple dynamic contact angle model’, *Proceedings of the 21st Australasian Fluid Mechanics Conference*, 10–13 December, Adelaide, Australia.

Malgarinos, I., Nikolopoulos, N., Marengo, M., Antonini, C. and Gavaises, M. (2015) ‘VOF simulations of the contact angle dynamics during the drop spreading: standard models and a new wetting force model’, *Advances in Colloid and Interface Science*, Vol. 212, pp.1–20.

Muradoglu, M. and Tasoglu, S. (2010) ‘A front-tracking method for computational modeling of impact and spreading of viscous droplets on solid walls’, *Computers & Fluids*, Vol. 39, No. 4, pp.615–625.

OpenFOAM User Guide Version 1.6 (2009) Open CFD Ltd. [online] https://sourceforge.net/projects/foam/files/foam/1.6/ (accessed 31 May 2019).

Popinet, S. and Zaleski, S. (1999) ‘A front-tracking algorithm for accurate representation of surface tension’, *International Journal for Numerical Methods in Fluids*, Vol. 30, No. 6, pp.775–793.

Raeini, A.Q., Blunt, M.J. and Bijeljic, B. (2012) ‘Modelling two-phase flow in porous media at the pore scale using the volume-of-fluid method’, *Journal of Computational Physics*, Vol. 231, No. 17, pp.5653–5668.

Roisman, I.V., Opfer, L., Tropea, C., Raessi, M., Mostaghimi, J. and Chandra, S. (2008) ‘Drop impact onto a dry surface: role of the dynamic contact angle’, *Colloids and Surfaces A: Physicochemical and Engineering Aspects*, Vol. 322, Nos. 1–3, pp.183–191.

Šikalo, Š., Wihelm, H-D., Roisman, I.V., Jakirlić, S. and Tropea, C. (2005) ‘Dynamic contact angle of spreading droplets: experiments and simulations’, *Physics of Fluids*, Vol. 17, No. 6, pp.062103-1–13.

Strella, S. (1970) ‘Analysis of spreading of a viscous drop on a smooth surface’, *Journal of Applied Physics*, Vol. 41, No. 10, pp.4242–4243.

Tanner, L.H. (1979) ‘The spreading of silicone oil drops on horizontal surfaces’, *Journal of Physics D: Applied Physics*, Vol. 12, No. 9, pp.1473–1484.

Wörner, M. (2012) 'Numerical modeling of multiphase flows in microfluidics and micro process engineering: a review of methods and applications', *Microfluidics and Nanofluidics*, Vol. 12, No. 6, pp.841–886.

Yokoi, K. (2014) 'A density-scaled continuum surface force model within a balanced force formulation', *Journal of Computational Physics*, Vol. 278, pp.221–228.

Yokoi, K., Vadillo, D., Hinch, J. and Hutchings, I. (2009) 'Numerical studies of the influence of the dynamic contact angle on a droplet impacting on a dry surface', *Physics of Fluids*, Vol. 21, No. 7, pp.072102-1–12.

Nomenclature

Ca	Capillary number
$C_{\mathbf{n}}$	Relaxation parameter for interface normal smoothing
$C_{\mathbf{u}}$	Relaxation parameter for velocity smoothing
C_κ	Parameter for α_{sm} in curvature computation
d_{cl}	Spreading diameter of circular contact line
$\mathbf{f}_{\text{c}}$	Capillary forces
$\mathbf{g}, g$	Gravity vector, gravitational acceleration
h	Mesh size
$N_{\mathbf{n}}$	Number of iterations for interface normal smoothing
$N_{\mathbf{u}}$	Number of iterations for velocity smoothing
N_κ	Iterations for α_{sm} in curvature computation
$\mathbf{n}_1$	Interface normal
p	Pressure
R	Radius
S	Cell face area
Δt	Time step size
t	Time
$\mathbf{u}$	Velocity (vector)
u	Velocity (magnitude)
V	Volume

Greek letters

α	Liquid volume fraction
δ_{b}	Regularised Dirac delta function
Γ	Boundary
κ	Interface curvature
μ	Dynamic viscosity
ϕ	Volumetric flux
σ	Surface tension
θ	Contact angle
Ω	Fluid domain

Subscripts

$1, 2$	Phase indices
c	Capillary
$\text{c} \to \text{f}$	Interpolation from cell to face centres
cl	Contact line
d	Dynamic
e	Equilibrium
$\text{f} \to \text{c}$	Interpolation from face to cell centres
$\text{f} \to \text{v}$	Interpolation from face centres to vertices
m	Volume averaged value
P	Cell centre
sc	Spurious currents
sh	Sharpened field
sm	Smoothed field
$\text{v} \to \text{f}$	Interpolation from vertices to face centres
w	Wall (substrate)
YL	Young-Laplace